Detecting planets around active stars: impact of magnetic fields on radial velocities and line bisectors

É. M. Hébrard,[1,2]★ J.-F. Donati,[1,2] X. Delfosse,[3] J. Morin,[4,5] I. Boisse,[6] C. Moutou[6,7] and G. Hébrard[8,9]

[1]*CNRS-INSU, IRAP-UMR 5277, 14 Av. E. Belin, F-31400 Toulouse, France*
[2]*Université de Toulouse, UPS-OMP, IRAP, F-31400 Toulouse, France*
[3]*UJF-Grenoble 1/CNRS-INSU, IPAG UMR 5274, F-38041 Grenoble, France*
[4]*LUPM, Université Montpellier II, CNRS, UMR 5299, Place E. Bataillon, F-34095 Montpellier, France*
[5]*Institut für Astrophysik, Georg-August-Universität, Göttingen, Friedrich-Hund-Platz 1, D-37077 Göttingen, Germany*
[6]*Aix-Marseille Université, CNRS, LAM, UMR 7326, F-13388 Marseille, France*
[7]*CNRS, Canada-France-Hawaii Telescope Corporation, 65-1238 Mamalahoa Hwy, Kamuela, HI 96743, USA*
[8]*IAP, Université Pierre et Marie Curie, UMR 7095 CNRS, 98 bis bd. Arago, F-75014 Paris, France*
[9]*Observatoire de Haute-Provence, CNRS/OAMP, F-04870 St Michel l'Observatoire, France*

ABSTRACT

Although technically challenging, detecting Earth-like planets around very low mass stars is in principle accessible to the existing velocimeters of highest radial-velocity (RV) precision. However, low-mass stars being active, they often feature dark spots and magnetic regions at their surfaces generating a noise level in RV curves (called activity jitter) that can severely limit our practical ability at detecting Earth-like planets. Whereas the impact of dark spots on RV data has been extensively studied in the literature, that of magnetic features only received little attention up to now. In this paper, we aim at quantifying the impact of magnetic fields (and the Zeeman broadening they induce) on line profiles, line bisectors and RV data. With a simple model, we quantitatively study the RV signals and bisector distortions that small magnetic regions or global magnetic dipoles can generate, especially at infrared wavelengths where the Zeeman broadening is much larger than that in the visible. We report in particular that the impact of magnetic features on line bisectors can be different from that of cool spots when the rotational broadening is comparable to or larger than the Zeeman broadening; more specifically, we find in this case that the top and bottom sections of the bisectors are anticorrelated, i.e. the opposite behaviour of what is observed for cool spots. We finally suggest new options to show and ultimately filter the impact of the magnetic activity on RV curves.

Key words: line: profiles – techniques: polarimetric – techniques: radial velocities – stars: magnetic field – starspots.

1 INTRODUCTION

Most exoplanets known today were detected thanks to the so-called radial-velocity (RV) technique. This method measures the periodic RV variations of a star that result from the reflex motion induced by an orbiting planet. These small variations are detectable through Doppler shifts of the whole spectrum. RVs are usually obtained by computing the cross-correlation function (CCF) of the observed spectrum with a reference spectrum. With the improvement of spectroscopic techniques and the construction of ultra-stable échelle spectrographs (called velocimeters), RV precisions of better than $1\,\mathrm{m\,s^{-1}}$ can be reached on long time-scales, rendering the detection

of Super-Earths and Earth-like planets a priori possible (e.g. Pepe et al. 2011; Dumusque et al. 2012).

To ease the detectability of such planets, an interesting option is to study the cooler, less massive and much more numerous M dwarfs. Not only their RV curves are comparatively more sensitive to the presence of exoplanets, but they vastly dominate the stellar population in the solar neighbourhood and are likely hosting most planets in our Galaxy. Their reduced temperatures move their habitable zones closer in, further increasing RV signals from potential habitable exoplanets (four times for M4), and easily allowing complementary studies, like transit observations.

However, M dwarfs are often active. Stellar activity (e.g. spots, granulation, magnetic fields) can impact the shape of stellar spectral lines and thus induce apparent RV variations mimicking those induced by an orbiting planet (e.g. Queloz et al. 2001), called RV jitter.

★ E-mail: elodie.hebrard@irap.omp.eu

The activity level depends on both the mass and the rotation period of the star (Morin et al. 2008b). M dwarfs with rotation periods in the range 15–40 d produce typical activity jitters of 3–20 m s^{-1} – enough to drown RV signals from potential exoplanets (e.g. Bonfils et al. 2007; Forveille et al. 2009). To avoid misinterpreting RV data and to improve the detection threshold, it is crucial to accurately characterize the impact of stellar activity on usual proxies such as line bisectors.

As mentioned already, RV jitter results from the presence of inhomogeneities at the surface of the star, carried across the visible disc by rotation and impacting the position and shape of line profiles. By analysing in detail the shape of spectral lines, one can distinguish planetary signals from activity jitters. Existing studies on RV jitters (such as Queloz et al. 2001; Desort et al. 2007; Meunier, Desort & Lagrange 2010; Reiners et al. 2010; Barnes, Jeffers & Jones 2011; Boisse et al. 2011) mainly focus on the impact of cool/dark spots, and of convective blueshifts in Sun-like stars. They show that spots can impact in various ways RVs and line bisectors depending on the characteristics of the spot and the star. In particular, they find that in the case of surface brightness inhomogeneities, there is an anticorrelation between the RV signal and the bisector slope. A chromatic dependence of the RV jitter is also expected, and might help distinguishing RV signatures from planets and from magnetic activity. Finally, for Sun-like stars, the blueshifted contribution of convective upflows associated with granulation dominates the observed RV signal, generating typical jitters of a few m s^{-1}.

A recent study focuses on the impact of magnetic fields on RV measurements (Reiners et al. 2013). They conclude that magnetic regions can significantly distort near-IR (nIR) stellar line profiles through Zeeman broadening and therefore affect RV measurements at the ∼1 m s^{-1} level in visible domain for magnetic regions with fields of ∼600 G covering ∼3 per cent of the visible stellar disc. More exhaustive studies on the RV impact of stellar magnetic fields and their topologies are needed, describing in particular how Zeeman broadening distorts line positions and shapes.

In this paper, we quantify through simulations the impact of dark spots and magnetic regions on spectral lines, for stars of various parameters. In Section 2, we outline the framework of our simulations. In Section 3, we validate our toy model by comparing our results with those of previous published studies. We estimate their effects on the observables commonly used in the analysis of RV data, i.e. RV curves, bisectors shape and their temporal evolution. Then in Section 4, we study more specifically the impact of a magnetic region or dipole on both RVs and line bisectors under the effect of the Zeeman broadening. In Section 5, we conclude our study by summarizing our results and by suggesting new avenues to diagnose the impact, and eventually filter out the effect of magnetic activity on the RV curves of active stars.

2 DESCRIPTION OF SIMULATIONS

2.1 Star and spectrum modelling

We model the stellar surface by dividing it into a dense grid with a large number of cells (typically 10 000). We compute the synthetic spectral line at a given rotation phase by adding the spectral contribution of all cells, taking into account their locations at the surface of the star and the local characteristics of the atmosphere (brightness, magnetic field, velocity field). This synthetic stellar line is taken as the equivalent of the observed CCF.

To describe the local line profile from each grid cell, we use the Unno–Rachkovski analytical solution of the radiative transfer

Table 1. Parameters used in simulations.

Main line modelling parameters	Symbol	Value
Doppler broadening	$\Delta\lambda_D$	1.6 km s^{-1}
Damping constant	a	0.1
Opacity ratio	η_0	2.0
Slope of Planck function	c	3.0
Linear limb darkening	ϵ	0.6
Landé factor	g	1.2
Spot parameters	**Symbol**	**Range**
Size	f_t	1 per cent
Latitude	θ	0°–90°
Phase	ϕ	0–1
Relative brightness	b	0–1
Magnetic field	B_{spot} or B_{dipole}	0–2200 G
Magnetic dipole inclination	β	60°
Star parameters	**Symbol**	**Range**
Projected rotation velocity	$v\sin i$	2–14 km s^{-1}
Stellar inclination	i	0°–90°

equation for polarized light (Unno 1956), assuming a plane-parallel Milne–Eddington atmosphere. In this context, the profile depends on five parameters, the Doppler width $\Delta\lambda_D$, the damping constant a, the ratio of the opacity at line centre to that in continuum η_0, the slope of the Planck function with continuum optical depth c, the linear limb-darkening coefficient ϵ and the line magnetic sensitivity characterized by the Landé factor g (see the first panel of Table 1). This simple solution is known to provide a good description of line profiles in the presence of magnetic fields and/or dark/cool spots (Skumanich & Lites 1987). The spectral contribution of each cell also depends on the local brightness b relative to that of the unspotted photosphere (i.e. with $b = 0.0$ and $b = 1.0$, respectively, corresponding to no light emission and to the unspotted photosphere); we simply assume that the continuum linearly scales with b and that the profile shape remains constant. It depends as well on the local magnetic field vector, distorting the line profile and generating polarization signatures according to the Zeeman effect and following Unno–Rachkovski's analytical description. This description of the local profile slightly differs from those implemented in previous studies (e.g. Boisse, Bonfils & Santos 2012); however, it has little influence on the impact of dark spots on line profiles, while allowing us to take into account the distorting effects of magnetic fields.

Inhomogeneities (i.e. dark spots and/or magnetic regions) on the stellar surface are assumed to be circular with a relative size f_t, given by

$$f_t = \frac{1 - \cos(\alpha)}{2}, \qquad (1)$$

where α is the semi-angle under which the spot is seen from the centre of the star.[1] They are characterized (see the second panel of Table 1) by their latitude θ, their rotation phase ϕ at which they cross the sub-observer meridian, their relative brightness b (<1 for a dark spot), and their magnetic strength and orientation. We also consider the particular case of a pure dipole field (see Section 4.7)

---

[1] Note that previous papers use other definitions: for example Boisse et al. (2012) or Reiners et al. (2013) use f_r, the fractional area of the visible hemisphere covered by a spot or a magnetic field, verifying for small values of α: $f_r = 2f_t$.

Table 2. Notations used.

RV curve	V_r
RV curve semi-amplitude	K
Average velocity of the top part of the bisector	V_t
Average velocity of the bottom part of the bisector	V_b
Velocity span curve ($V_t - V_b$)	V_s
Velocity span curve semi-amplitude	J

defined by its polar field strength B_{dipole} and its tilt with respect to the rotation axis β.

To derive the synthetic spectral line from the whole star at each rotation phase, we simply sum up the spectral contributions of all cells, taking into account the inclination angle of the star to the line of sight i and the line-of-sight projected equatorial rotation velocity $v \sin i$ (see the third panel of Table 1). We finally normalize the resulting synthetic spectral profile to a unit continuum. For a non-rotating star, this synthetic profile has a full width at half-maximum (FWHM) of $5.6 \, \mathrm{km \, s^{-1}}$ for an instrumental spectral resolving power of 75 000 [similar to that of the SOPHIE velocimeter on the 1.9 m telescope of Observatoire de Haute-Provence, of the ESPaDOnS spectropolarimeter on the 3.6 m Canada–France–Hawaii Telescope (CFHT) and of SPIRou, the next-generation nIR spectropolarimeter/high-precision velocimeter for CFHT].

2.2 RV and bisectors computations

RVs are computed by fitting a Gaussian to the synthetic profiles generated with our toy model, the Gaussian centroid giving the RV estimate V_r. To derive the bisector, we first interpolate the synthetic profile using a cubic spline interpolation; we then compute the set of mid-points of horizontal line segments extending across the profile (Gray 1982). To assess the line shape evolution, we calculate the velocity span (as introduced, e.g. by Gray 1982; Queloz et al. 2001) V_s, given by $V_t - V_b$, where V_t and V_b are, respectively, the average velocity at the top and bottom part of the bisector.[2]

The semi-amplitudes of the variations of V_r and V_s with rotation phases are denoted as K and J, respectively.

All the notations used afterwards are summarized in Table 2.

3 EFFECT OF DARK SPOTS

Like in previous RV studies (Desort et al. 2007; Reiners et al. 2010; Boisse et al. 2012), we start by simulating the impact of dark spots on line profiles to validate our toy model. In this aim, we consider a star with a single dark spot, compute V_r, V_s, V_b and V_t (see Table 2) at 100 evenly spread phases across the rotation cycle, and look for their temporal variations, for different spot and star parameters.

3.1 Impact of an equatorial spot

We first consider an equatorial spot, having $b = 0.0$ (i.e. emitting no light) with a relative area of $f_t = 1$ per cent, on a star with $v \sin i = 5 \, \mathrm{km \, s^{-1}}$, and viewed equator-on (i.e. $i = 90°$), as shown in Fig. 1 (top panel).

The spot induces a distortion in the line profile, and thus a corresponding RV shift and bisector tilt. As the star rotates and the spot is carried across the visible disc (see e.g. the five selected phases,

---

[2] The top and bottom parts include all points within 10–40 and 60–90 per cent of the full line depth, respectively.

labelled A–E, highlighted in the top panel of Fig. 1), this distortion travels through the line profile. The resulting V_r and V_s curves are shown in Fig. 1 (bottom panel, left and right curves, respectively); their semi-amplitudes (denoted as K and J) are, respectively, equal to 130 and $110 \, \mathrm{m \, s^{-1}}$, in good agreement with previous results (e.g. Boisse et al. 2012). The shape of the bisector at phases A–E is depicted in Fig. 2 (left-hand panel). As expected, we observe that the line distortion induced by the spot is mostly local, i.e. is mainly affecting the line wings when the spot is on the stellar limb (phases A and E), and the line core when the spot is close to the centre of the visible stellar disc (phases B and D).

Plotting V_s as a function of V_r produces a dual-loop diagram (see the middle panel in Fig. 2), similar to those of Desort et al. (2007). We note that this diagram is different from what we expect for a planet (for which $V_s = 0$ for all values of V_r); more specifically, we observe that V_r and V_s are anticorrelated. This well-known result is commonly used to diagnose activity jitter (e.g. Queloz et al. 2001).

Looking at how V_b varies with V_t, we obtain a similar dual-loop diagram (see the right-hand panel of Fig. 2) with both quantities being now correlated rather than anticorrelated. The reason behind this is easy to understand; wherever the dark spot is located on the visible stellar disc, both bottom and top parts of the bisector are shifted in the same direction (though by different amounts), so that V_b and V_t always have the same sign. Once again, we can check that this behaviour is different from what we expect in the case of a planet (i.e. $V_b = V_t$).

3.2 Impact of $v \sin i$

We now consider a set of models with $v \sin i$ ranging from 2 to $14 \, \mathrm{km \, s^{-1}}$ (all other parameters remaining constant). We find that V_r and V_s increase with $v \sin i$. More specifically, in the investigated range of $v \sin i$, K is found to be almost linear with $v \sin i$ and f_t, whereas J varies linearly with f_t and quadratically with $v \sin i$, consistent with Desort et al. (2007) or Boisse et al. (2012) despite the slight difference in modelling the intrinsic profile.

Looking at how V_s varies with V_r (see the left-hand panel of Fig. 3), we note that similar diagrams are obtained for all values of $v \sin i$, with V_s being largely anticorrelated with V_r. The main changes in these plots concern the average slope of the correlation as well as the amplitude of the loop, both with increasing $v \sin i$. As expected, when $v \sin i$ is smaller than the intrinsic spectral line width, we observe that V_s remains small for all values of V_r; in this case, there is little to no difference between spectral distortions induced by a spot and those due to a planet. The bisector is thus no longer a relevant proxy of stellar activity at low $v \sin i$, in agreement with previously published studies (e.g. Desort et al. 2007; Boisse et al. 2012).

We also observe that V_b and V_t are always correlated (see the right-hand panel in Fig. 3). As in the previous case, the average correlation slope and the loop amplitude of the plots both decrease with decreasing $v \sin i$, until the whole diagram merges on to the first diagonal (for $v \sin i < 5 \, \mathrm{km \, s^{-1}}$), making it impossible to distinguish planetary signals from RV jitters.

The larger the $v \sin i$, the stronger the correlation induced by the Doppler effect between the location of the spot at the stellar surface and the velocity of the corresponding distortion in the line profile. As a result, for $v \sin i$ higher than $\sim 10 \, \mathrm{km \, s^{-1}}$, variations of V_b with respect to V_t exhibit two increasingly distinct successive stages:

(i) one with V_b varying while V_t remains almost constant and much smaller than V_b, i.e. when the spot is close to the centre of the

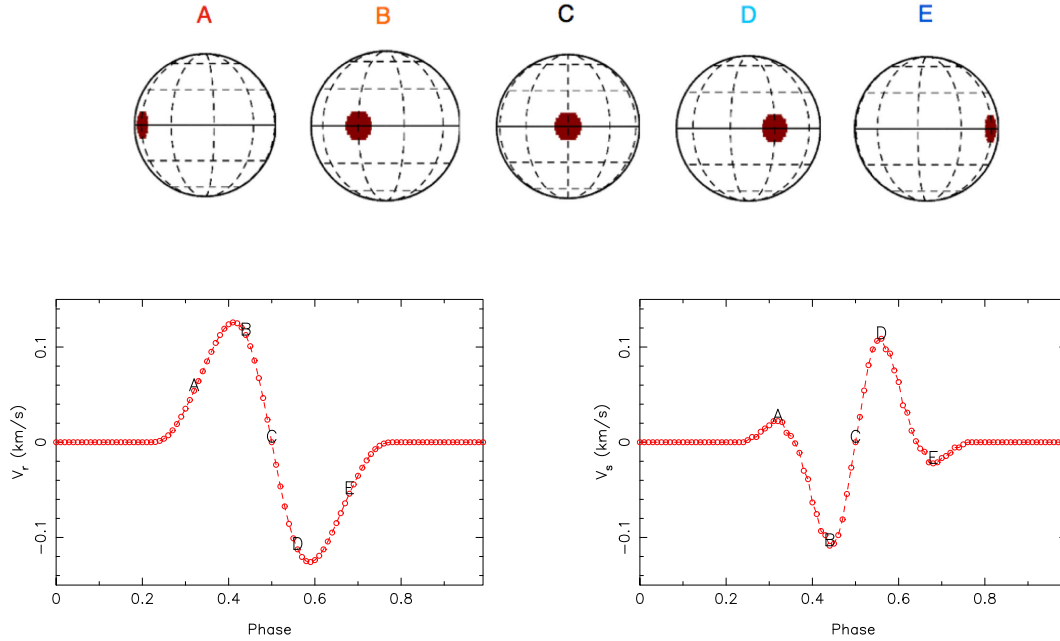**Figure 1.** Impact of a dark spot on V_r and V_s, for a star with $i = 90°$ and $v \sin i = 5$ km s^{-1}, and for a dark spot with $b = 0$ covering 1 per cent of the stellar surface. The top panel represents the spot location with respect to the line of sight at five rotation phases labelled A–E and corresponding to phases 0.32, 0.44, 0.50, 0.56 and 0.68. The bottom panel shows the temporal variations of V_r (bottom left) and V_s (bottom right).
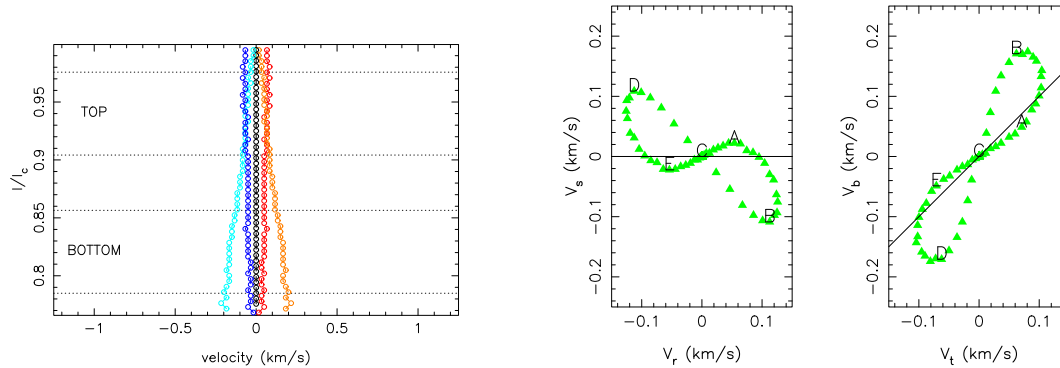

Figure 2. Left-hand panel: lines bisector in the case of a star with a dark spot and for phases A–E (same star/spot and colour code as in Fig. 1, top panel). The dashed lines represent the boundaries for the computation of V_b and V_t. Middle and right-hand panels: variations of V_s as a function of V_r, and V_b as a function of V_t, respectively, for the same star and spot as described previously in Fig. 1. Phases A–E refer to those highlighted in Fig. 1. The straight lines depict the variations of V_s as a function of V_r and V_b as a function of V_t expected in the case of RV changes induced by planets (rather than by dark spots).

visible stellar disc; this corresponds to rotational phases B–D, i.e. when the bottom part of the bisector is most affected (see Fig. 4);

(ii) another one during which the opposite behaviour is observed, with V_t varying while V_b remains almost constant and much smaller than V_t, i.e. when the spot is close to the stellar limb; this corresponds to rotational phases A and E, i.e. when the top part of the bisector is most affected (see Fig. 4).

On the dual-loop diagram of Fig. 3 (right-hand panel), these two successive stages graphically correspond to a vertical, and then to a horizontal migration of the point that depicts the line profile variations as the star rotates. We also observe that the amplitude of V_b variations largely exceeds that of V_t variations, directly reflecting the fact that the spot is best visible to the observer when crossing the stellar disc.

3.3 Impact of i and θ

We now study the impact of θ and i on the line profile variations, considering a spot with $\theta = 0°$ or $\theta = 60°$, and a star with $i = 90°$ or with $i = 30°$; we also assume $v \sin i = 5$ km s^{-1}, $b = 0$ and $f_t = 1$ per cent (see Fig. 5, top panel).

Looking at how V_s varies with V_r, and V_b with V_t (see Fig. 5, bottom-left and bottom-right panels, respectively), we note that θ mostly impacts the loop width of the dual-loop diagrams, with flatter loops observers at higher latitudes. For example if $\theta = 60°$, the loop is flattest, i.e. V_s and V_r (respectively, V_b and V_t) vary almost in phase, because the line profile distortion remains in the line core.

Similarly, we observe that i affects the amplitude of the loops. If the spot stays close to the stellar limb whenever visible (Fig. 5, second and third figures of the top panel), the amplitude of the loop is small; on the opposite, if the spot comes close to the visible
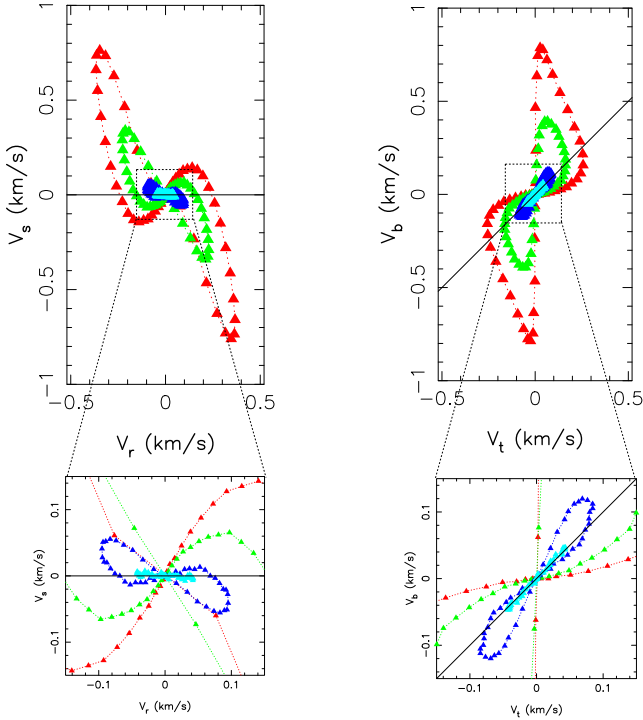
Figure 3. V_s as a function of V_r and V_b as a function of V_t for four different $v \sin i$: $2\,\mathrm{km\,s^{-1}}$ (turquoise), $4\,\mathrm{km\,s^{-1}}$ (blue), $8\,\mathrm{km\,s^{-1}}$ (green) and $12\,\mathrm{km\,s^{-1}}$ (red). The star is viewed equator-on with an equatorial spot covering 1 per cent of the stellar surface with $b = 0$. The straight lines represent the variations of V_s as a function of V_r and V_b as a function of V_t for RV changes induced by a planetary companion (rather than by a dark spot). The bottom part represents a zoom of diagrams around $\pm 0.15\,\mathrm{km\,s^{-1}}$.
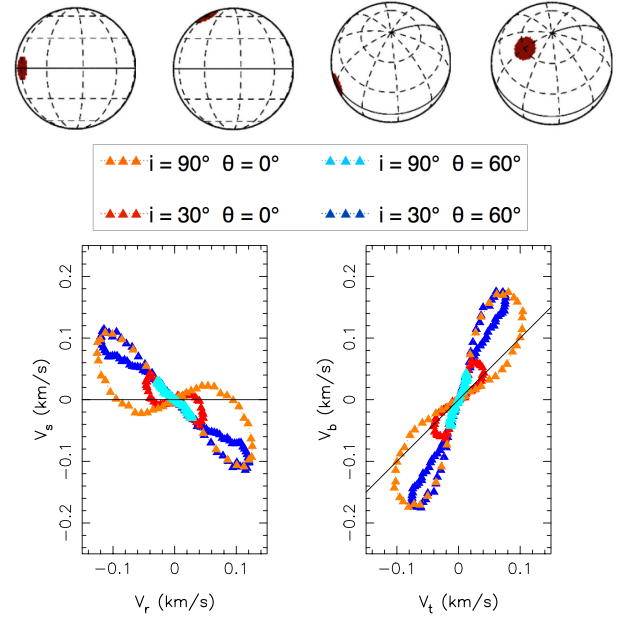
Figure 5. Top panel: different star/spot configurations considered in Section 3.3, assuming a star with $v \sin i = 5\,\mathrm{km\ s^{-1}}$ and a spot with $f_t = 1$ per cent. From left to right: $i = 90°$ and $\theta = 0°$, $i = 90°$ and $\theta = 60°$, $i = 30°$ and $\theta = 0°$ and $i = 30°$ and $\theta = 60°$. Bottom panel: evolution of V_s as a function of V_r (left) and V_b as a function of V_t (right) for each of the four cases shown in the top panel. The straight lines are as defined in Fig. 2.
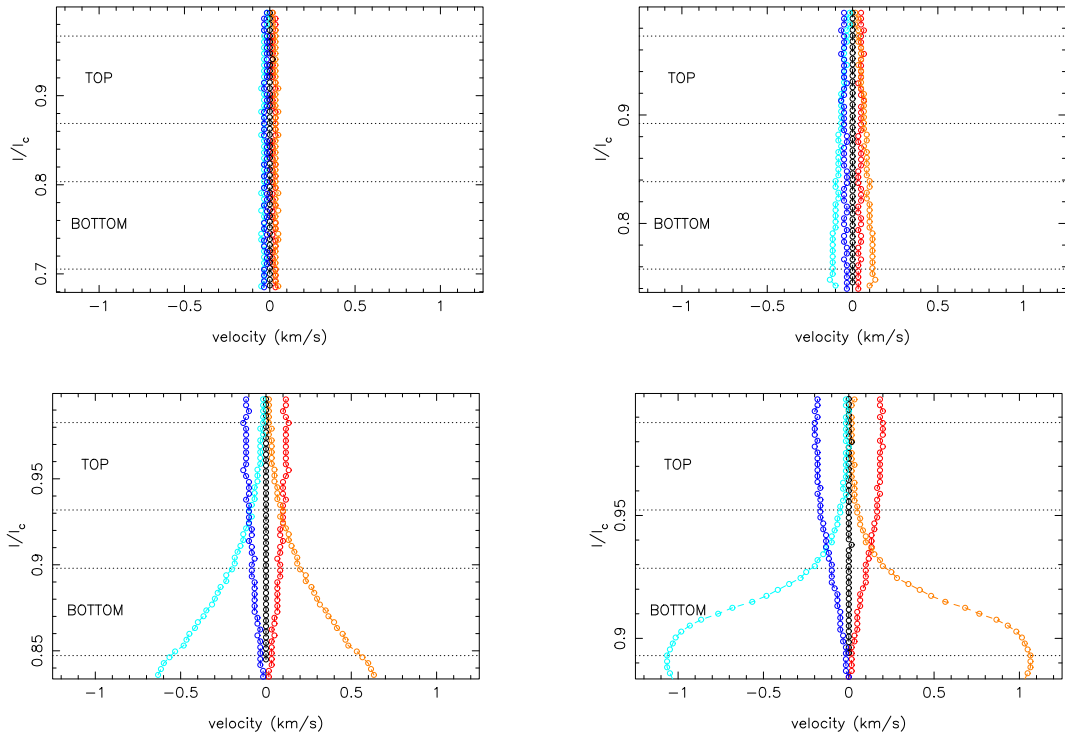

Figure 4. Impact of $v \sin i$ on the bisector shape. The star/spot parameters are as defined in Fig. 1, except for $v \sin i$, now set to 2, 4, 8 and $12\,\mathrm{km\,s^{-1}}$ for the top-left, top-right, bottom-left and bottom-right panels. The colour code is the same as defined in Fig. 1 (i.e. red for phase A, orange for phase B, dark for phase C, turquoise for phase D and blue for phase E). The dashed lines point out the boundaries for the computation of V_b and V_t.

stellar disc throughout its transit, the loop amplitude is large. Finally, contrary to $v \sin i$, i and θ do not impact the average slope of the correlation between V_s and V_r or V_b and V_t.

3.4 Impact of the contrast and the wavelength

In the previous sections, we assumed a spot with $b = 0$. If we now consider a spot with $b > 0$, as is the case of real spots on real stars, b would then vary with wavelength, depending on the temperatures of the spots and of the photosphere. According to our current knowledge, spots of cool stars are known to exhibit a temperature contrast with respect to the surrounding quiet photosphere ranging from ~2000 K in G stars to ~200 K in M dwarfs (Berdyugina 2005).

As a result of the temperature dependence of the local profile continuum and shape, profile distortions induced by cool spots are in most cases shallower in the infrared than those in the visible, reflecting the smaller spot-to-photosphere brightness contrast. According to observations, the RV jitter can be up to approximately four times smaller in the nIR than in the visible (e.g. Martín et al. 2006; Huélamo et al. 2008; Prato et al. 2008; Mahmud et al. 2011). This chromatic dependence of K and J may be used as an additional proxy to distinguish RV jitter induced by cool spot from planetary signals; this effect is larger for M dwarfs than for G stars as a result of the lower photospheric temperature and spot-to-photosphere temperature contrast.

4 EFFECT OF MAGNETIC FIELDS

Stellar activity phenomena in low-mass stars are mostly powered by magnetic fields. These fields can be detected through their impact on stellar spectra, and more specifically through the broadening and polarization they generate within line profiles via the Zeeman effect. A recent paper used simulations to study, for the first time, RV signatures caused by magnetic regions on stellar surfaces (Reiners et al. 2013). In the present study, we expand these initial tests using our toy model, and further consider the impact of surface magnetic features on line bisectors and on their temporal evolution. Since magnetic fields do not only concentrate within dark spots but can also be found in regions at photospheric temperature (both in stars, see e.g. Donati et al. 1999; Morin et al. 2008a, and in the Sun, see e.g. Buehler, Lagg & Solanki 2013), we start by considering a single magnetic region. We then compute V_r, V_s, V_t and V_b as described in Section 2.2. We also compare our results with those of Reiners et al. (2013) whenever relevant. Then we consider in a second step the two additional cases of a cool magnetic spot (Section 4.6) and of a large-scale magnetic dipole (Section 4.7).

4.1 The Zeeman effect

In the presence of a magnetic field, spectral lines split into several sub-components gathering in three main groups, called the σ_b, π and σ_r components. Each group is characterized by a specific polarization, left-handed/right-handed circular polarization for σ_b/σ_r components (in the specific case of absorption lines) and linear polarization for π components.

Hereafter we assume the simple case of a normal Zeeman triplet, in which only three sub-components show up, one blueshifted σ_b component at wavelength $\lambda_0 - \Delta\lambda_B$, one central π component at wavelength λ_0 and one redshifted σ_r component at wavelength $\lambda_0 +$

$\Delta\lambda_B$, where λ_0 is the central rest wavelength of the unperturbed line, and $\Delta\lambda_B$ is given by

$$\Delta\lambda_B = 4.67 \times 10^{-12}\lambda_0^2 gB, \qquad (2)$$

with λ_0 in nm and B in Gauss. The parameter g, called Landé factor, describes the sensitivity of the line to magnetic fields. In terms of velocity, this shift corresponds to

$$\Delta v_B = 1.40 \times 10^{-3}\lambda_0 gB, \qquad (3)$$

with v in m s^{-1}. For example, the Zeeman splitting for $B = 1$ kG and $g = 1.2$ at 0.5 μm is $\Delta\lambda_B = 1.4 \times 10^{-3}$ nm or $\Delta v_B = 0.84$ km s^{-1} while we have at 2.2 μm $\Delta\lambda_B = 27 \times 10^{-3}$ nm or $\Delta v_B = 3.7$ km s^{-1}. Equation (3) shows that the Zeeman splitting and thus the broadening of spectral lines that results increases when the magnetic field intensity B and the rest wavelength λ_0 increase.[3]

The relative intensity of the three sub-components of the normal Zeeman triplet, as well as their apparent polarization states, depends on the magnetic field orientation with respect to the line of sight.

4.2 Impact of an equatorial magnetic region

We first consider a circular magnetic region with a radial magnetic field of 1.8 kG, a relative area of $f_t = 1$ per cent, on a star viewed equator-on with $v \sin i = 5$ km s^{-1} as shown in the top panel of Fig. 6. We carry out the study at 2.2 μm, where the Zeeman splitting is larger than that in the visible domain ($\Delta v_B = 6.6$ km s^{-1} for $B = 1.8$ kG and $g = 1.2$).

The local line profile from the cells affected by the magnetic field is broadened by the Zeeman effect, getting deeper in the wings and shallower in the core. This broadening induces a global distortion of the synthetic line profile integrated over the whole visible stellar hemisphere; more specifically, this profile distortion can extend on a much wider wavelength interval (depending on the magnetic strength) than in the case of a dark spot.

As the star rotates, the magnetic region is carried across the visible disc (see Fig. 6, top panel), and the induced distortion travels through the line profile, affecting most of the time both wings and core. This crossing induces a corresponding RV shift as well as a distortion of the bisector. The resulting V_r and V_s curves are shown in the lower panel of Fig. 6 (left and right curves respectively), with semi-amplitudes of ~140 m s^{-1}.

The shape of the bisector and its temporal evolution are shown in Fig. 7 (left-hand panel). As expected, we observe that the distortion induced by the magnetic region is different from that caused by a dark spot; more specifically, we observe that the highest section of the bisector (corresponding to 0–10 per cent of the full line depth) is much more affected most of the time, reflecting that the profile is now also impacted in the far wings. Moreover, we note that this highest section is shifted in a direction opposite to the bottom part. Besides, we also observe that, when the bottom part of the bisector is affected, the top part is impacted too, much more than in the case of a distortion due to a cool spot.

Despite these differences, the variations of V_s as a function of V_r, as well as those of V_b as a function of V_t (see Fig. 7, middle and right-hand panel, respectively), remain similar, showing again

---

[3] This example mostly refers to atomic lines; for molecular lines, abundant in the spectrum of M dwarfs, results may differ depending on their Zeeman sensitivity (possibly lower than that of atomic lines in average; e.g. Reiners et al. 2013). Landé factors of molecular lines are however poorly known at the moment, with few laboratory measurements yet available in particular.
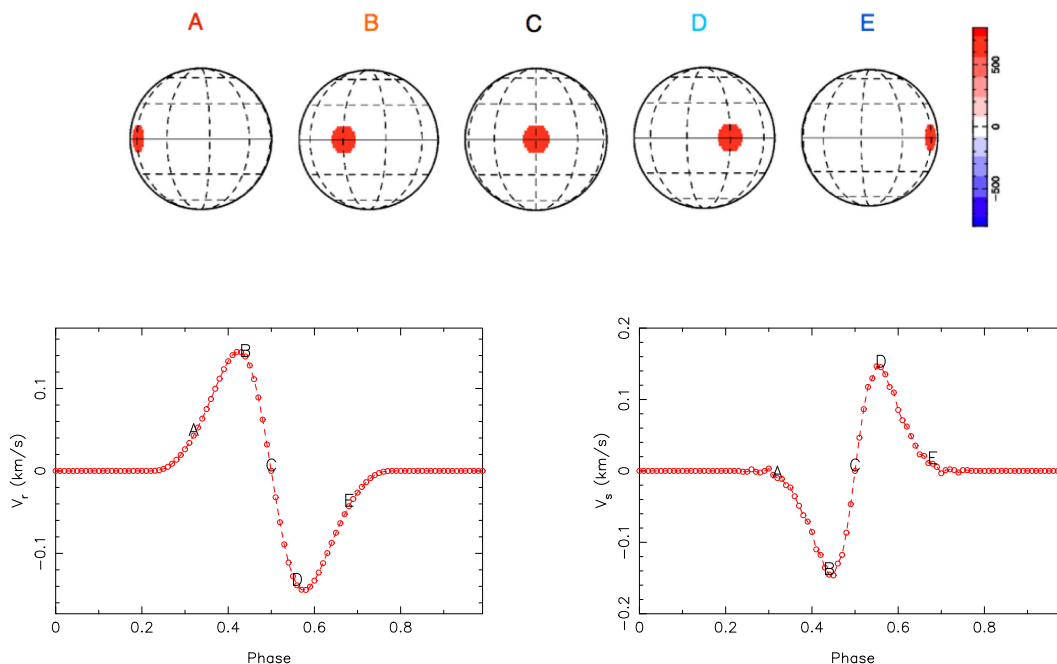
Figure 6. Same as Fig. 1 except for the spot, now being a magnetic region with a radial field of 1.8 kG. The line central wavelength is set to $\lambda_0 = 2.2\ \mu$m.
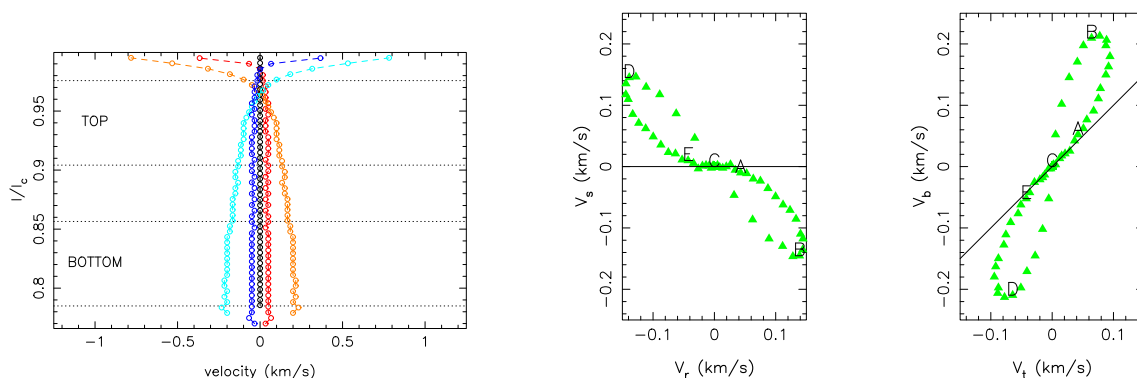

Figure 7. Same as Fig. 2 but now for the synthetic star and magnetic topology shown in Fig. 6.

a dual-loop diagram. V_s versus V_r (respectively V_b versus V_t) are again largely anticorrelated (respectively correlated) – the largest difference occurring near phases A and E, i.e. when the magnetic region is at the far limb. Both diagrams are still different from what we expect for a planetary companion.

To better emphasize the differences between line profile distortions caused by a magnetic region and a cool spot, respectively, we show dynamic spectra of profile residuals for both cases (see Fig. 8) – residuals being computed as the difference between the distorted line profiles and the undistorted ones (corresponding to a quiet photosphere). We clearly observe that the profile wings and far wings (as far as $\pm 12\ \mathrm{km\,s^{-1}}$) are much more affected in the case of a magnetic region than in the case of a cool spot, for which the profile distortions mostly concentrate within $\pm v \sin i$ (i.e. $\pm 5\ \mathrm{km\,s^{-1}}$). This suggests that dynamic spectra contain more information about profile distortions than line bisectors, even at low $v \sin i$, and could be used as a complementary tool to diagnose the effect to a magnetic region on RV curves.

4.3 Impact of $v \sin i$

We now consider a star with $v \sin i$ ranging from 2 to $14\ \mathrm{km\,s^{-1}}$, all other parameters remaining constant. This amounts to varying the ratio of the $v \sin i$ to the Zeeman splitting from 0.3 to 1.8.

We find that, in the investigated range of $v \sin i$, K no longer varies linearly, as it used to be in the case of a dark spot; more specifically, we observe that K reaches a maximum at about $8\ \mathrm{km\,s^{-1}}$ before slowly decreasing for higher rotation rates (see Fig. 9).

Similarly, J shows an inflection point at about the same value of $v \sin i$; at lower values of $v \sin i$, J varies almost quadratically with $v \sin i$ as was the case for cool spots. To better understand the variations of K and J with $v \sin i$, we outline below the bisector evolution for four different values of $v \sin i$ ranging from 2 to $12\ \mathrm{km\,s^{-1}}$ (see also Fig. 11).

(i) For $v \sin i = 2\ \mathrm{km\,s^{-1}}$, we observe that, whatever the rotation phase, the bisector is almost constant and remains vertical (centred on zero), except in the far wings, i.e. in regions not contributing to
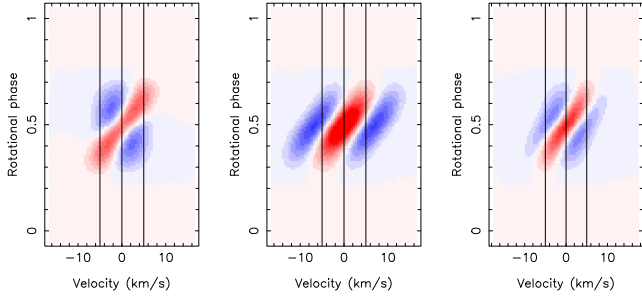
Figure 8. Dynamic spectra of the line profile residual in the case of a cool spot ($b = 0$ and $B = 0$ kG, left-hand panel), of a magnetic region at photospheric temperature ($b = 1$ and $B = 1.8$ kG, middle panel), and of a cool magnetic spot ($b = 0.6$ and $B = 1$ kG, left-hand panel). From left to right, the vertical lines correspond to velocity of $-v \sin i$, 0 and $+v \sin i$. Each horizontal strip of this image corresponds to a colour-coded difference spectrum at a given rotation phase, with blue and red respectively standing for differences of -10 and $+10$ per cent. The characteristics of the star and of cool/magnetic spot are as mentioned in Figs 1 and 6.
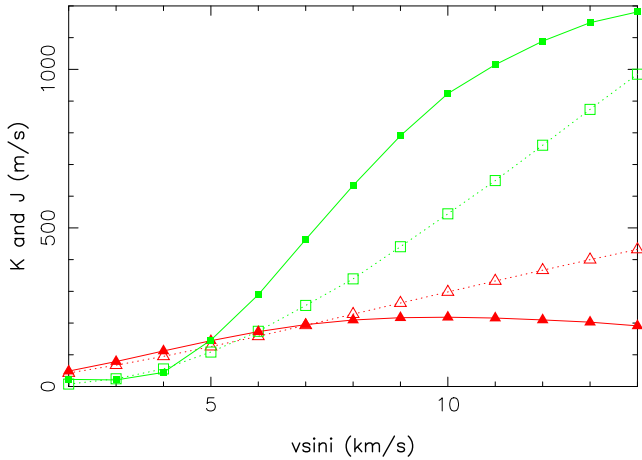
Figure 9. Variation of K (red triangles) and J (green squares) with $v \sin i$ for the same star/magnetic area parameters as defined in Fig. 6 (filled symbols and solid line) and for the same star/spot parameters as defined in Fig. 1 (open symbols and dotted line).

V_b and V_t. Most of the information about the magnetic region is lost and both K and J remain close to zero. As a result, variations of V_r, V_s, V_b and V_t closely mimic those expected in the case of a planet (see Fig. 10, left- and right-hand panels).

(ii) For $v \sin i = 4$ km s^{-1}, the bisector is still mostly vertical, except again in the upper section, but globally shifted by up to ± 100 m s^{-1} when the magnetic region is close to the centre of the visible stellar disc (phases B and D). We also note that V_b has the same sign as V_t at all times, with V_b slightly larger than V_t. In this case, V_b remains correlated with V_t (respectively V_s anticorrelated V_r), but both are still very close to the variations expected in the case of a planet (Fig. 10).

(iii) For $v \sin i = 8$ km s^{-1}, the slope of the bisector gets much higher at phases B and D. In particular, the crossing point of bisectors at phases B and D is now located in the top section of the bisector, so that V_t and V_b have opposite signs. The distortion affects more or less equally both the top and bottom parts of the bisectors. The dual-loop diagrams are significantly impacted, and no more compatible with what we expect for a planet. The slope of V_s versus V_r (see Fig. 10, left-hand panel) is much larger than in the case of a dark spot (see Fig. 3, left-hand panel), whereas V_b is now even anti-
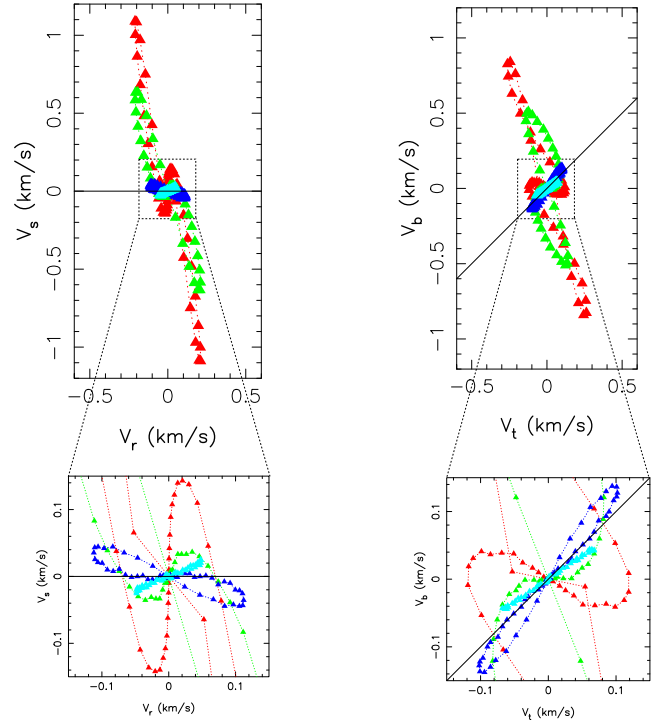

Figure 10. Same as in Fig. 3, but for the star and magnetic region shown in Fig. 6.

correlated with V_t (see Fig. 10, right-hand panel) and not correlated as in the case of dark spots (see Fig. 3, right-hand panel).

(iv) For $v \sin i = 12$ km s^{-1}, the bisector is strongly affected at most rotation phases when the magnetic region is visible, with a bottom part much more impacted (V_b reaching almost ± 900 m s^{-1}) than the top part (± 250 m s^{-1}). The crossing point between bisectors at phases B and D now reaches the lower section of the bisector, while the top part is more or less vertical. Both dual-loop diagrams have a larger amplitude than, but otherwise similar shape to, the case with $v \sin i = 8$ km s^{-1}, with V_b again strongly anticorrelated with V_t (see Fig. 10).

This demonstrates that both the bisector shape evolution and the correlation between V_b and V_t strongly depend on the ratio between the $v \sin i$ and the Zeeman splitting. When $v \sin i$ is similar to or larger than the Zeeman splitting (equal to $\sim$6.6 km s^{-1} in our example, see Section 4.2), V_b is anticorrelated with V_t and the evolution of V_r, V_s, V_b and V_t with $v \sin i$ is different from that found for dark spots.

4.4 Impact of magnetic field strength and wavelength

To further assess the impact of the Zeeman broadening on the line profile, we now examine how the profile variations react to changing the field strength of the magnetic region shown in Fig. 6.

At 1.8 kG (Fig. 7), although the π component affects the profile core, the σ components only impact the far wings due to the much larger Δv_B with respect to $v \sin i$. As a result, both bottom and top parts of the bisector are shifted in the same direction, making V_b and V_t correlated. This is why the effect of the magnetic region on the line profile is comparable to the impact of a dark spot. However, if the magnetic field strength decreases, Δv_B decreases too while the FWHM of the rotationally broadened line remains constant ($\sim$8.5 km s^{-1} at $v \sin i = 5$ km s^{-1}). The full magnetic
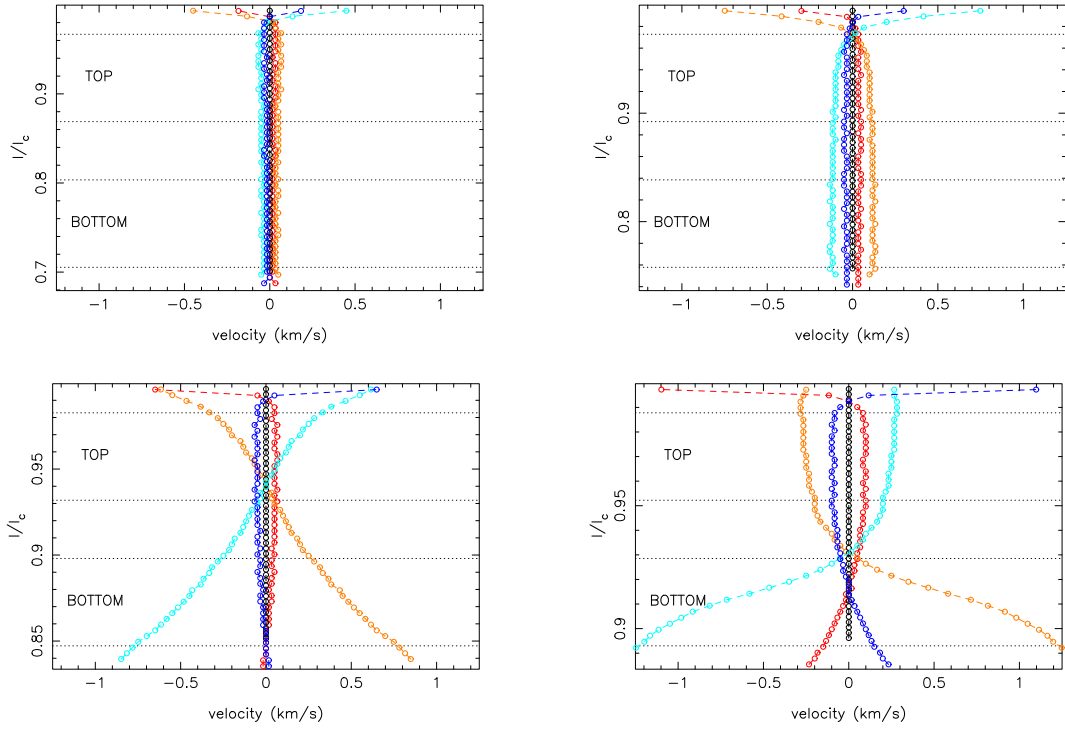
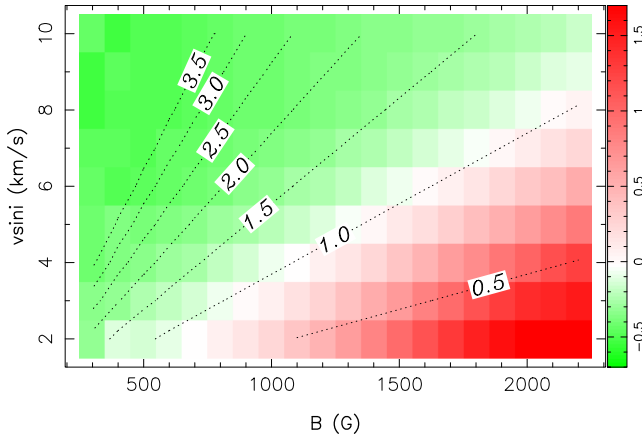**Figure 11.** Same as Fig. 4 but for the star and magnetic region shown in Fig. 6.

Figure 12. Effect of $v \sin i$ and B on the average slope of V_t as a function of V_b. Red corresponds to a correlation, whereas green corresponds to an anticorrelation. The other characteristics of the star and the magnetic region are as given in the caption of Fig. 6. Dotted lines trace contours of constant $\frac{v \sin i}{\Delta v_B}$.
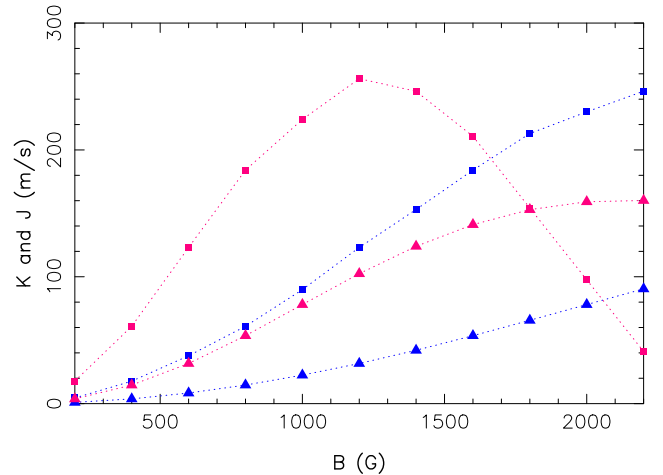

Figure 13. Evolution of K (triangle) and J (square) with the magnetic field intensity varying from 200 G to 2.2 kG. Blue curves (respectively pink curves) are for a wavelength of 1.1 μm (respectively 2.2 μm). The star and the magnetic region are as described in the caption of Fig. 6.

distortion (i.e. both π and σ components) can affect the whole profile (10–90 per cent of the full line depth), so that V_b and V_t are affected simultaneously with opposite signs (anticorrelation). One can observe a similar anticorrelation at 1.8 kG when increasing $v \sin i$ to, e.g. 8 km s^{-1} (see Fig. 10, right-hand panel), with the top and bottom parts of the bisectors shifted most of the time in opposite directions (see Fig. 11, bottom-left panel).

To further investigate the impact of $v \sin i$ and B on the correlation of V_b versus V_t, we compute the average correlation slope between these two parameters, with $v \sin i$ and B in the range 2–10 km s^{-1} and 0.3–2.2 kG, respectively (see Fig. 12).

We observe that V_b is anticorrelated with V_t, when $v \sin i$ is similar to or larger than Δv_B ($\frac{v \sin i}{\Delta v_B} \geq 1.0$). We note that this change in the

correlation between V_b and V_t also corresponds to an evolution of how J varies with B and $v \sin i$. For example, at $v \sin i = 5$ km s^{-1} and $\lambda_0 = 2.2$ μm, we find that J reaches a maximum at 1.3 kG (Fig. 13), i.e. the value of B at which the correlation switches sign (Fig. 12).

Furthermore, B and λ_0 have a similar impact on the line profile, as expected from equation (3). For instance, at 1.1 μm, J reaches its maximum at 2.6 kG. A multiwavelength analysis thus has the potential to help us discriminate the physical origin of the line profile variations, and more specifically whether they are caused by a planet, a dark spot and/or a magnetic region.
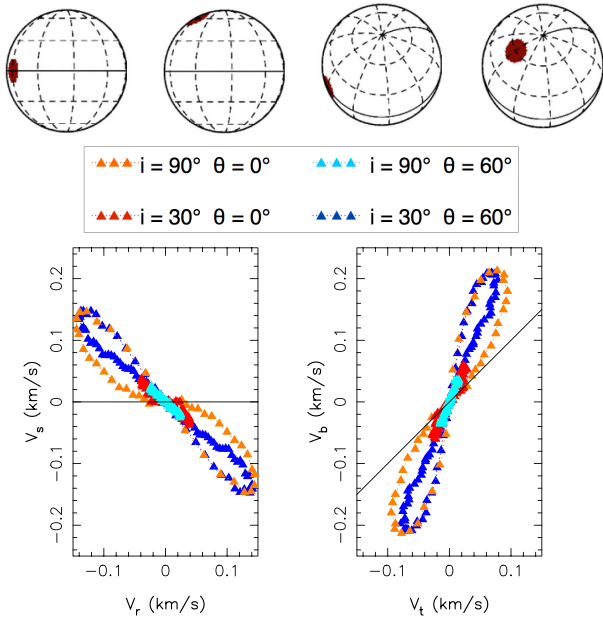
Figure 14. Same as Fig. 5, but on a star with $v \sin i = 5\,\mathrm{km\,s^{-1}}$ and magnetic region of $f_t = 1$ per cent with $B = 1.8$ kG.

In addition, we find that K no longer grows when Δv_B gets comparable to the FWHM of the rotationally broadened line, as found in Reiners et al. (2013). Assuming an equatorial magnetic region with a radial field of 1 kG and covering $f_t = 2.5$ per cent on a star viewed equator-on with a $v \sin i$ of $2\,\mathrm{km\,s^{-1}}$, we find that $K \sim 24\,\mathrm{m\,s^{-1}}$ at 1.2 µm, fully compatible with the value of $25\,\mathrm{m\,s^{-1}}$ reported in Reiners et al. (2013). We also confirm that K grows linearly with f_t, and quadratically with λ_0 and B (Reiners et al. 2013): whereas for an equatorial magnetic zone of $f_t = 1.5$ per cent and $B = 500$ G, at 2.2 µm, $K = 17.1\,\mathrm{m\,s^{-1}}$, at 1.1 µm, $K = 4.5\,\mathrm{m\,s^{-1}}$.

4.5 Impact of i and θ

As in Section 3.3, we briefly examine the impact of i and θ on the line profile, distinguishing again the same four cases (see Fig. 14, top panel). Looking at how V_s varies with V_r, and V_b with V_t (see Fig. 14, bottom-left and bottom-right panels, respectively), we note very similar behaviour as in the case of a dark spot (see Fig. 5); θ mostly affects the loop width, whereas i impacts their amplitudes.

4.6 Impact of a magnetic cool spot

We now briefly study the case of a cool magnetic spot. For M dwarfs, the temperature difference between the quiet photosphere and the spot is typically 450 K, and rarely exceeds 900 K (Berdyugina 2005). In this case, modelling both the photosphere and the spot as blackbodies, the relative spot brightness is likely to be $b \sim 0.75$, and is always larger than $b \sim 0.55$ at 2.2 µm. To investigate the combined effects of brightness and magnetic fields, we compute the average correlation slope between V_b and V_t, with b and B, respectively, in the range 0–1 and 0.3–2.2 kG (see Fig. 15). When b ranges from 0.8 to 1.0, the effect of B on the line bisector dominates for magnetic fields weaker than 1.0–1.4 kG (this threshold depending on $v \sin i$ as explained in Section 4.4). For instance, V_t is anticorrelated with V_b for a magnetic field of $B = 0.9$ kG at $b = 0.75$ (i.e. corresponding to a temperature difference of 450 K
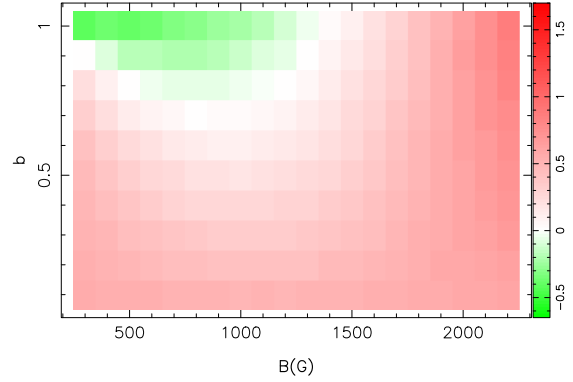

Figure 15. Effect of b and B on the average slope of V_t as a function of V_b for a cool magnetic equatorial spot on an equator-on star with $v \sin i = 5\,\mathrm{km\,s^{-1}}$ at 2.2 µm (same colour code as in Fig. 12).

for a photospheric temperature of 3700 K). However, when b is smaller than ~ 0.6, V_b is always correlated with V_t. The effect of the brightness contrast on the line bisector largely dominates that of magnetic field – the Zeeman signatures being too faint to generate a detectable impact. In this case, we note that the dynamic spectrum still includes information on the magnetic field in the far wings and significantly differs from that corresponding to a non-magnetic dark spot (see Fig. 8, left- and right-hand panels).

4.7 Example of a magnetic dipole

We finally consider the case of a magnetic dipole similar to those often found at the surfaces of fully convective M dwarfs (see e.g. Morin et al. 2008b). We assume a star viewed at $i = 60°$ with $v \sin i = 5\,\mathrm{km\,s^{-1}}$, hosting a 0.6 kG magnetic dipole tilted at $\beta = 60°$ (see Fig. 16, top panel). As both magnetic poles are not viewed under the same angle at closest approach (see the top panel of Fig. 16), their respective signatures in V_r and V_s are different, with the pole coming closest to the observer (positive pole) generating the largest signals.

Looking at how V_s varies with V_r, we again note an anticorrelation between these two parameters (Fig. 17, middle panel), with the corresponding dual-loop diagram now showing a simpler, almost linear, shape. Similarly, V_b is tightly anticorrelated with V_t (Fig. 17, right-hand panel). As in Section 4.3, $v \sin i$ controls the slope of V_s versus V_r and V_b versus V_t diagrams (see Fig. 18); as $v \sin i$ increases, the tight anticorrelations differ more and more from those expected in the case of a planetary companion. We observe the same behaviour whatever i and β – these two parameters impacting only the loop amplitude. Furthermore, we report that K is 3 times smaller than J at $\lambda_0 = 2.2$ µm (see Fig. 16, bottom-left and bottom-right panels), and that both K and J are ~ 15 times smaller at 0.55 µm than at 2.2 µm (see Fig. 18).

The temporal evolution of the bisector (Fig. 17, left-hand panel) shows that both top and bottom parts have opposite signs at all rotation phases. This behaviour is somewhat reminiscent of what is observed for some specific magnetic regions and stellar parameters, more specifically, those corresponding to the green domain of Fig. 12. Among the various notable differences, the main one is that both parameters tightly correlate with each other in the case of a dipole, reflecting that the bisectors corresponding to all rotation phases now cross each other at almost the same line depth.

The main origin of these differences is that, in the case of a dipole, the whole stellar surface (rather than just a small area) is covered
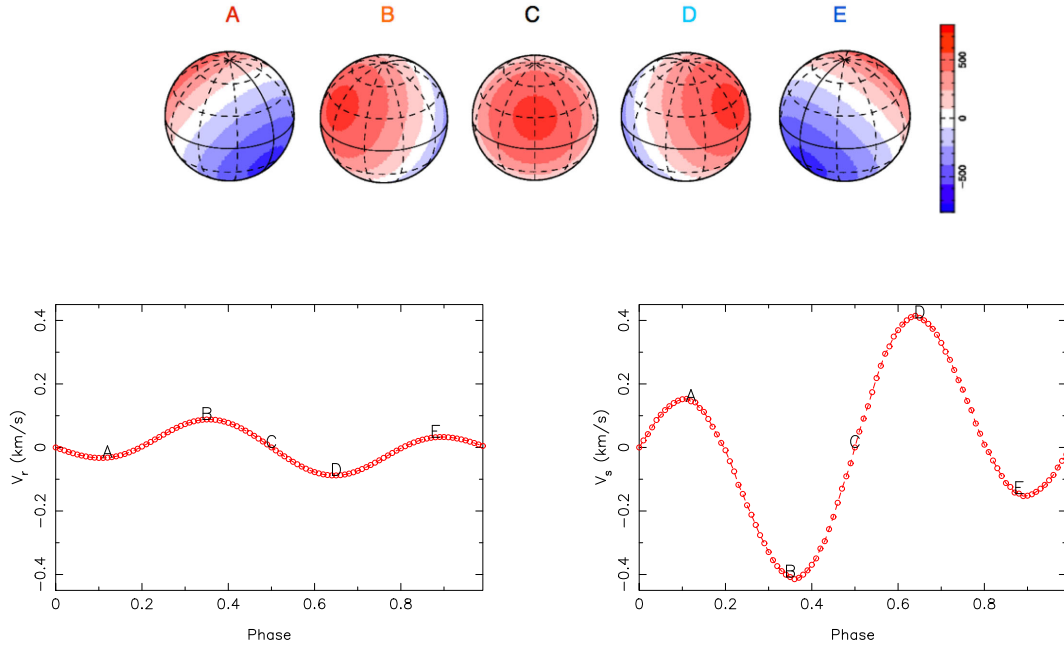
Figure 16. Same as Fig. 6 but with a star inclined at $i = 60°$ and hosting a 0.6 kG magnetic dipole tilted at $\beta = 60°$ to the rotation axis. Phases A – E now, respectively, correspond to phases 0.12, 0.35, 0.50, 0.65 and 0.88.
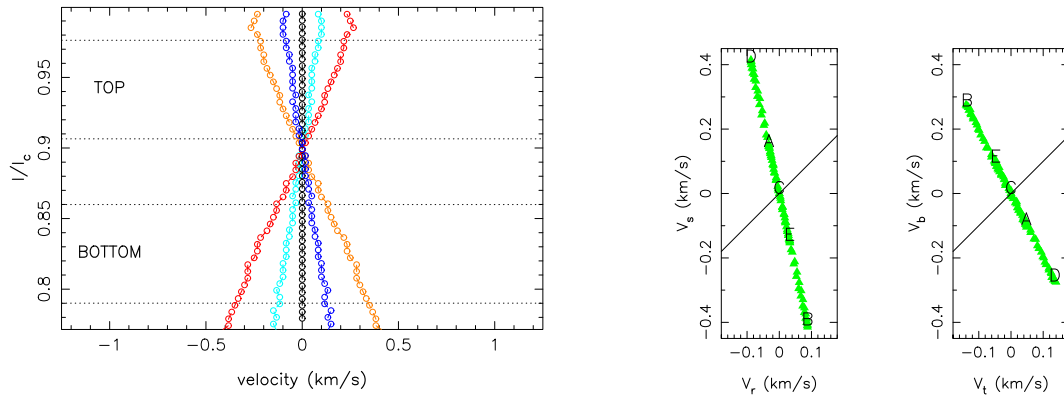

Figure 17. Same as Fig. 2, but for the star and magnetic topology shown in Fig. 16.

with magnetic fields whose intensity varies from 50 to 100 per cent of the polar field strength, depending on the magnetic latitude. As a result, the line bisector is distorted most of the time rather than only within a restricted phase range; moreover, the range of the surface magnetic strengths ensures that the σ components now span a wider velocity interval, thus affecting the profile on a larger scale.

5 SUMMARY AND PERSPECTIVES

In this paper, we studied the impact of magnetic activity on both RV measurements and line profile bisectors – concentrating first on dark spots, and then on magnetic features of various types. More specifically, we investigated how magnetic regions affect the radial velocity V_r, the bisector span V_s, as well as the average velocity of the bottom, V_b, and top, V_t, part of the bisector depending on a number of key parameters (e.g. the projected rotation velocity $v \sin i$, the

stellar inclination i, the inhomogeneity latitude θ, the magnetic field strength B, the central wavelength of the study λ_0). We also looked at dynamic spectra to suggest new ways of diagnosing magnetic activity in line profile.

As already described in previous studies, dark spots distort line profiles, generating RV variations potentially mimicking a planetary signal and modifying the shape of line bisectors, in such a way that V_s and V_r are anticorrelated. In this new study, we focused more precisely on the bisector evolution as the star rotates, looking at how V_b varies with V_t. The distortion induced by a cool spot being mostly local (see Section 3.1), we find that V_b and V_t are correlated, for all stellar configurations and spot parameters.

We first studied the case of a magnetic field region at photospheric temperature, and then that of a cool magnetic spot. Magnetic regions have an effect on line profiles, especially at nIR wavelengths, showing both similarities and differences with the case of dark spots. In
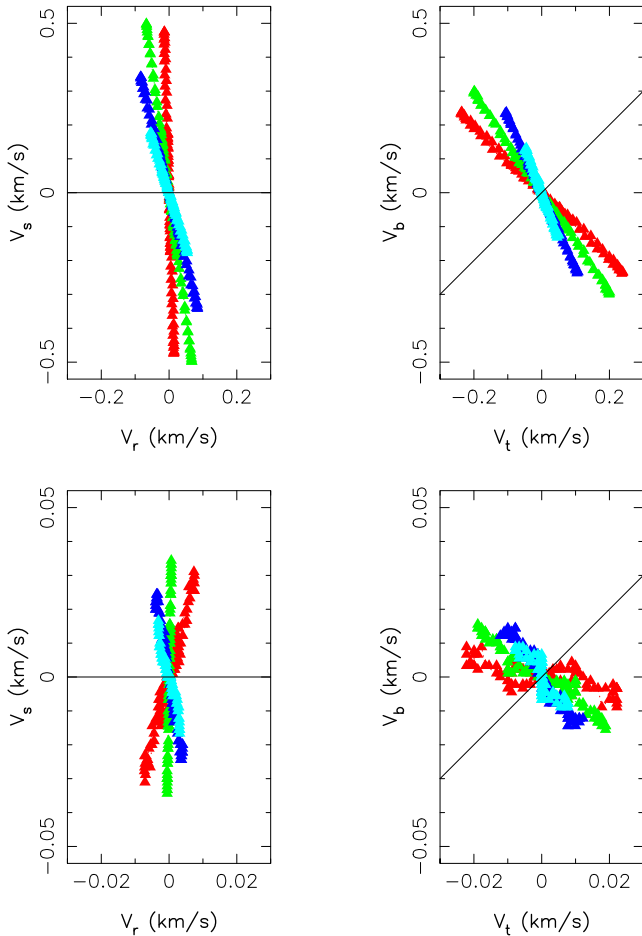
Figure 18. Same as in Fig. 3, but for a dipole with $B = 0.6$ G, $\beta = 60°$ and $i = 60°$, for $\lambda_0 = 2.2$ μm (top panel) and for $\lambda_0 = 0.55$ μm (bottom panel). Note the 10 times smaller horizontal and vertical scales for the bottom panel.

particular, although we always observe an anticorrelation between V_r and V_s, V_b and V_t can either be anticorrelated or correlated, depending on whether the Zeeman splitting is, respectively, smaller or larger than $v \sin i$. This anticorrelation is what differs most from the case of cool spots, and reflects that the Zeeman distortion affects simultaneously, but in opposite directions, V_b and V_t when the magnetic region crosses the centre of the visible hemisphere. Moreover, this change from anticorrelation to correlation occurs when J also reaches a maximum as a function of B (see Fig. 13), at a given λ_0 and $v \sin i$. As B and λ_0 play equivalent roles with respect to Δv_B, we find, as expected, that J reaches its maximum as a function of λ_0; beyond this maximum V_b and V_t become correlated.

We also report that, for a slow rotator, the effect of magnetic regions on V_s is much smaller than that on V_r (see Fig. 9), making difficult the use of bisectors to diagnose stellar activity as in the case of cool spots.

With a large-scale magnetic dipole, the whole star is magnetic; as a result the distortion affects the line profile at all rotation phases, so that V_b is always anticorrelated with V_t, for the different star/dipole parameters tested herein. Up to now, the usual proxy for disentangling genuine planetary RV signals from RV jitters (caused by either cool spots or magnetic regions) is the anticorrelation between V_s and V_r. We show in this paper that looking at the correlation between V_b and V_t can bring further information, allowing one to distin-

guish dark spots from magnetic regions in some specific cases (see Fig. 12) especially in the nIR. Moreover, we confirm that the impact of stellar magnetic regions on line profiles is wavelength dependent (Reiners et al. 2013), whereas that of a planet is achromatic. More specifically, with a dark spot, J and K decrease when λ_0 increases; on the opposite, both reach a maximum for a magnetic region. A multiwavelength study can thus allow one to determine the main origin of the activity jitter. In the case of a cool magnetic spot, the impact of a magnetic field on the bisector is only visible at low photosphere-to-spot brightness contrasts, i.e. mostly for M dwarfs in the nIR. Looking at dynamic spectra seems an interesting option to diagnose from line profiles the nature of the magnetic activity affecting RV curves.

The next step in our study is to implement a reliable way to invert sets of distorted profiles/dynamic spectra into maps of brightness/magnetic features, with the ultimate goal of filtering out the activity jitter from RV curves. This new filtering technique will have to preserve potential planetary signals. To further investigate this idea, we are presently carrying out RV and spectropolarimetric measurements at optical wavelengths with HARPSPol on the 3.6 m European Southern Observatory telescope on the one hand, and with both SOPHIE on the 1.93 m telescope at Observatoire de Haute-Provence and NARVAL on the 2 m telescope Bernard-Lyot atop Pic-du-Midi on the other hand.

Finally, this work also serves as science preparation for SPIRou – the next-generation spectropolarimeter/high-precision velocimeter for the 3.6 m CFHT – that will operate at nIR wavelength (first light in 2017).

REFERENCES

Barnes J., Jeffers S., Jones H., 2011, MNRAS, 412, 1599
Berdyugina S. V., 2005, Living Rev. Sol. Phys., 2, 8
Boisse I., Bouchy F., Hébrard G., Bonfils X., Santos N., Vauclair S., 2011, A&A, 528
Boisse I., Bonfils X., Santos N., 2012, A&A, 545
Bonfils X. et al., 2007, A&A, 474, 293
Buehler D., Lagg A., Solanki S., 2013, A&A, 555
Desort M., Lagrange A., Galland F., Udry S., Mayor M., 2007, A&A, 473, 983
Donati J., Collier Cameron A., Hussain G. A. J., Semel M., 1999, MNRAS, 302, 437
Dumusque X. et al., 2012, Nature, 491, 207
Forveille T. et al., 2009, A&A, 493, 645
Gray D. F., 1982, ApJ, 255, 200
Huélamo N. et al., 2008, A&A, 489, L9
Mahmud N., Crockett C., Johns-Krull C., Prato L., Hartigan P., Jaffe D. C. A. B., 2011, ApJ, 736
Martín E., Guenther E., Zapatero Osorio M., Bouy H., Wainscoat R., 2006, ApJ, 644, L75
Meunier N., Desort M., Lagrange A.-M., 2010, A&A, 512, A39
Morin J. et al., 2008a, MNRAS, 384, 77
Morin J. et al., 2008b, MNRAS, 390, 567

Pepe F. et al., 2011, A&A, 534, A58

Prato L., Huerta M., Johns-Krull C., Mahmud N., Jaffe D., Hartigan P., 2008, ApJ, 687, L103

Queloz D., Henry G., Sivan J., Baliunas S., Beuzit J., Donahue R., 2001, A&A, 379

Reiners A., Bean J., Hubert K., Dreizler S., Seifahrt A., 2010, ApJ, 710, 432

Reiners A., Shulyak D., Anglada-Escudé G., Jeffers S., Morin J., Zechmeister M., Kochuklov O., Piskunov N., 2013, A&A, 552

Skumanich A., Lites B., 1987, ApJ, 322, 473

Unno W., 1956, PASJ, 8, 108

This paper has been typeset from a TEX/LATEX file prepared by the author.